Powder Technology 438 (2024) 119658

Contents lists available at ScienceDirect

Powder Technology

journal homepage: www.journals.elsevier.com/powder-technology

Experimental study of a dense stream of particles impacting on an inclined surface

Shipu Han [a,b], Zhiwei Sun [a,b,*], Zhao Feng Tian [a,b], Alfonso Chinnici [a,b], Timothy Lau [c], Maurizio Troiano [d], Roberto Solimene [e], Piero Salatino [d], Graham J. Nathan [a,b]

[a] Centre for Energy Technology, The University of Adelaide, SA 5005, Australia
[b] School of Electrical and Mechanical Engineering, The University of Adelaide, SA 5005, Australia
[c] UniSA STEM, The University of South Australia, Mawson Lakes, SA 5095, Australia
[d] Dipartimento di Ingegneria Chimica, dei Materiali e della Produzione Industriale, niversità Udegli Studi di Napoli Federico II, Piazzale V. Tecchio 80, 80125 Napoli, Italy
[e] Istituto di Scienze e Tecnologie per l'Energia e la Mobilità Sostenibile (STEMS), Consiglio Nazionale delle Ricerche, Piazzale V. Tecchio 80, 80125 Napoli, Italy

HIGHLIGHTS

- Impact of high-loading particle-laden flows against inclined surfaces was measured.
- CoR, rebound velocity and angle were measured for a range of volume fractions.
- Formation of a particle layer on the surface was confirmed at high volume fractions.
- The layer absorbs energy for all impacts thereby affects the rebound process.
- The layer transfers momentum to accelerate impacting particles for oblique impacts.

GRAPHICAL ABSTRACT

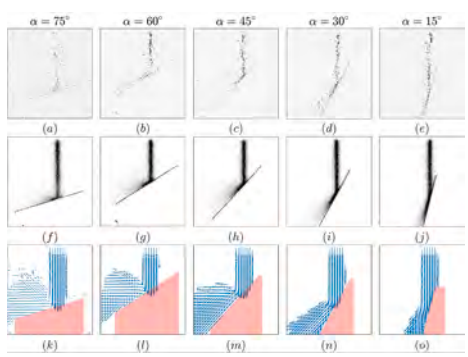

ARTICLE INFO

Keywords:
Particle-wall collision
Gravity-driven granular flow
Falling particle curtain
Rebound speed
Rebound angle
Coefficient of restitution

ABSTRACT

We present measurements of the impact process of gravity-driven flows of particles against inclined surfaces for a range of particle loadings in the four-way coupled regime. These were investigated with particle image velocimetry (PIV) for a range of particle curtain thicknesses, volume fractions, velocities and mass flow rates using a series of hoppers of various aperture sizes, following impact on a steel plate at a range of angles from 15° to 75°. In addition, micro-shadowgraphy was used to provide new details of the region of impact, providing the first direct evidence of the formation of layer of particles that slide along the surface for sufficiently high particle volume fractions. Statistical measurements of particle impact and rebound velocities, together with rebound angle and coefficient of restitution, were obtained from the PIV analysis, which revealed that an increase in particle loading leads to increase in the probability that a layer of particles at the surface is formed at the point of impact. This layer acts to absorb energy for all impact angles, thereby influencing the rebound processes. For impact angles close to the normal direction the layer also increases the range of rebound angles, while it causes particles to slide along the surface as a chute-like flow for large inclination angles.

* Corresponding author at: Centre for Energy Technology, The University of Adelaide, SA 5005, Australia.
E-mail address: zhiwei.sun@adelaide.edu.au (Z. Sun).

https://doi.org/10.1016/j.powtec.2024.119658
Received 27 October 2023; Received in revised form 29 January 2024; Accepted 13 March 2024
Available online 16 March 2024
0032-5910/© 2024 The Authors. Published by Elsevier B.V. This is an open access article under the CC BY license (http://creativecommons.org/licenses/by/4.0/).

1. Introduction

Gravity-driven flows of particles are widely employed in many industrial processes for production, handling and modification of particulate materials [1–3]. Numerical and experimental investigations have therefore been undertaken for various simplified flows of particles and gases to advance the understanding and improve the performance of these processes [4–6]. However, while freely-propagating flows have received considerable attention, far less has been given to the interaction of these flows with boundary walls. There is therefore a need to investigate interaction of particle flows with surfaces.

Interactions between particles and a surface can be characterised by the coefficient of restitution, e, for single particles, which is normally defined as the ratio of the rebound speed to the impact speed [7]. Many studies have been performed to measure or predict the coefficient of restitution for a wide range of particles and surfaces [8–11]. The effect of particle impact velocity [12], particle shape [13], surface roughness [14], surface inclination angle [15], and operating temperature [16,17] on both normal and oblique impacts have also been investigated extensively, both experimentally and numerically. The dynamics of single particles impacting on a surface are therefore generally well understood. However, this understanding is insufficient to allow reliable prediction of many two-phase flows of particles and gases, particularly where their volume fraction is sufficient to generate significant particle-particle interactions, owing to their much greater complexity. Such flows are typically classified as being four-way coupled, so that gas-to-particle, particle-to-gas and particle-to-particle interactions are all significant [18]. Therefore, there is an ongoing need for more understanding of dense streams of particles in this regime that impact on surfaces, for a range of inclination angles, to guide the development and validation of reliable models.

Both numerical modelling and experiments are required, with the former needed to understand the complex dynamics of particles impacting onto a surface, and the latter are needed for model development and validation. In particular, the absence of both direct measurements and modelling of particle-laden flows impacting onto a surface implies that new understanding is needed of the relative significance of various controlling parameters to assist in the development and validation of simplified models. Nevertheless, some insights can be gained from related fields. Gravity-driven granular flows, such as snow and rock avalanches, have been observed to deposit on the surface after impacting on a retaining wall to form a stagnant zone, which then significantly reduces the impact force applied to the retaining wall by absorbing some of the energy [19]. While part of the granular material forms a stagnant zone, an inertial layer of particles has also been observed to flow above the stagnant zone. This can result in tangential forces on the retaining wall and complex phenomena, such as direction reversal as the stagnant zone grows larger [19]. This previous work suggests that a stagnant layer and/or inertial layer of particles may also form under a continuous free-falling curtain of particles under some conditions, which would similarly inhibit the rebound of particles from a surface. However, while these qualitative description and explanations seem plausible, they are yet to be confirmed in falling curtains and there is also a need for quantitative data to increase understanding of them.

Furthermore, a particle flow down an inclined surface, also called a 'chute flow', can be significantly affected by the inclination angle of the surface [20]. For example, according to the Pouliquen flow rule [21], which describes the influence of the inclination angle and height, a chute flow can be sustained when its inclination angle is larger than the angle of repose. Although the layer of particles flowing down an inclined surface after impact is not a real chute flow, one can deduce that the inclination angle would also affect the status of such a layer, thereby influencing the rebound behaviour of the upstream particles. Moreover, a repulsive force generated by upstream particles during the impact could also be expected to affect the dynamics of the particle layer, thus changing the value of the critical angle. Hence, it is necessary to assess the effect of angles that change the flow regime of such a layer of particles after impact.

In addition to the particle layer, the significance of particle collisions within the flow also needs to be evaluated. Interactions between particles have been found to occur frequently at the upper part of a chute flow regardless of the inclination angle [22]. This implies that strong particle collisions are also likely to occur at the top of such a sliding particle layer. Furthermore, collisions between rebounding and incoming particles can also be expected to occur at small inclination angles when the layer is stagnant. Therefore, assessments of the effect of particle collisions on particle-laden flows impacting an inclined surface are needed.

In light of the discussion above, while impact processes of single particles and granular flows onto boundary walls have been relatively well studied, very limited attention has been paid to those of particle-laden flows within the four-way coupling regime, despite their wide application in industrial processes. In particular, understanding of the role of any particle layer and the significance of particle-particle interactions remains inadequate. Therefore, the overall aim of the present study is to quantify the behaviour of particles during the impact onto an inclined surface of particle-laden flows in the four-way coupling regime. More specifically, it aims to quantify the influence of particle volume fraction in the four-way coupling regime and inclination angle over the range of 15° to 75° on the rebound speed, rebound angle and coefficient of restitution.

2. Methodology

2.1. Experimental rig

Fig. 1a presents a schematic diagram of the experimental arrangement employed at The University of Adelaide, comprising an imaging system and a curtain of particles falling freely from a hopper with a rectangular orifice to impact onto an inclined surface at a range of inclination angles. The dimension of the chamber is $35 \times 35 \times 45$ cm^3. The target surface was glued to the top of a plate holder, which was 3D printed, and mounted at the centreline of the enclosure. The particle feeding hopper was mounted with a minimum distance above the target surface along the axis of 270 mm. As can be seen from Fig. 1b, the centre of the aperture of the hopper was defined as the origin of the coordinate system, while the positive directions of x and y axes were defined as the particle free-fall direction and that normal to the plane of rebound, respectively. The positive z direction was then defined by the right-hand rule.

Fig. 1c presents the coordinate system for the particle-wall collision, showing the particle impact velocity, $U_{p,i}$, particle rebound velocity, $V_{p,r}$, particle impact angle, α, inclination angle, $\theta = 90° - \alpha$, and particle rebound angle, Θ. Fig. 1d presents a snapshot of the particle curtain impacting on the target surface. It can be seen that significant dispersion of particles occurs in the y-z plane from the point of impact. The lateral dispersion angle, β, defines the spread of particles on the target surface that are out of the plane of the laser sheet and so are not recorded with the imaging system.

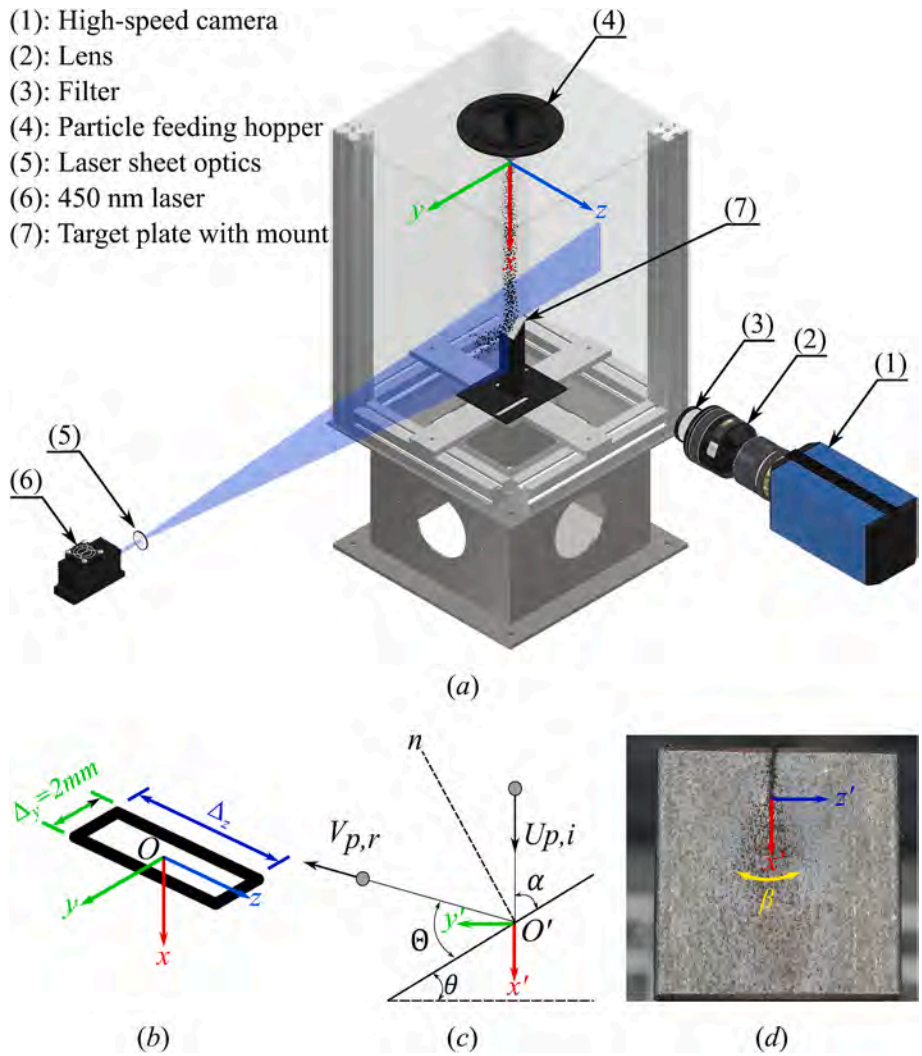

Fig. 1. (a) Schematic diagram of the experimental arrangement and the coordinate system; (b) the aperture at the bottom of the hopper, whose centre is the origin of the coordinate system; (c) particle-wall collision configuration with particle impact velocity, $U_{p,i}$, particle rebound velocity $V_{p,r}$, impact angle, α, inclination angle, $\theta = 90 - \alpha$, and rebound angle, Θ; and (d) single-shot image, viewed normal to the plate, of the particle-laden flow impacting on the surface, showing the lateral dispersion angle β.

2.2. Hoppers, particles and target surface

The particle discharge hopper was T-pyramid-shaped and configured to accommodate four alternative sizes of slot aperture at the exit plane to generate particle flows with various mass flow rates and, thereby, a range of volume fractions in the region-of-interest. The dimensions of the hopper aperture spanned 1.5 mm to 5 mm, generating mass flow rates between 0.25 and 2.39 g/s, as shown in Table 1. Carbo CP 70/140 particles (from Carbo Ceramics Inc.) were used for all the cases with a median diameter of d_p = 154 μm, a size distribution with 95% of diameters within the range of 105 μm – 212 μm [23], and a density of ρ_p = 3250 kg/m^3. Carbo CP particles were tested as they are commonly used as a solar absorption medium in new generation concentrating solar particle receivers [6]. Details of the particle can be found in the Appendix A. Stainless steel plates with No. 1 surface finish were used as the target surface, with an arithmetical mean height of the surface roughness, S_a = 5.8 μm, as measured with a profilometer, consistent with the nominal surface roughness of 3–6 μm for this finish. The size of the plate is approximately 30 × 30 mm^2. More information about the roughness of target plates can be found in the Appendix B. Since the particle median diameter to surface roughness ratio, $d_p/S_a \approx 26$, the influence of the surface roughness on the impact is assumed to be negligible.

Table 1
Experimental conditions.

Case	Free-drop height, H, [mm]	Hopper aperture size $\Delta_z \times \Delta_y$, [mm × mm]	Mass flow rate, $\dot{m}_{p,i}$, [g/s]	Impact angle, α, [°]
H270A1.5:	270	1.5 × 2	0.25	75; 60; 45; 30; 15
H270A2.0:		2.0 × 2	0.43	
H270A2.5:		2.5 × 2	0.70	
H270A5.0:		5.0 × 2	2.39	45
H550A2.5:	550	2.5 × 2	0.70	75; 60; 45; 30; 15

2.3. Optical methods and arrangement

Two types of optical arrangements, namely PIV and shadowgraphy, were used in the experiment. For the PIV arrangement, a high-power semiconductor laser with a wavelength of 450 nm from CivilLaser was used. The laser was operated at its maximum power capacity of 4 W for all measurements and triggered externally to operate in a dual-pulse mode with a repetition frequency of 1 Hz. The duration of each pulse

was 10 μs while the time delay between the dual pulses was 200 μs, resulting in an energy of 40 μJ per pulse. Two cylindrical lenses were placed into the laser beam to generate a laser sheet, whose position was carefully adjusted before each measurement to align it with the centre of the particle curtain, i.e., at $z = 0$. Normal to the laser sheet, particles were imaged using a lens (AF-S DX, Nikkor) onto a dual-frame PIV camera (PCO.2000, 2048×2048 pixels) that was synchronized with the laser. This arrangement has a field-of-view of 35×35 mm^2, corresponding to 17 μm/pixel, allowing both impact and rebound particles, together with the side view of the target surface, to be captured on each image. A bandpass filter (centred at 450 nm with a bandwidth of 10 nm) was placed in front of the imaging lens to reject any potential stray light sources and the lab lights were also switched off to maximize signal-to-noise ratio. At least 300 image pairs were collected for each experimental condition to ensure enough data for PIV analysis.

For the shadowgraphy arrangement, the same laser was used as the light source while an engineered diffuser (Thorlabs, ED1-C20-MD) was put into the laser beam to generate the back-light-field. The dual-frame PCO camera and the back-light were aligned in-line along the z direction and synchronized. A Mitutoyo microscopic lens (3x, magnification) was used to provide a smaller field-of-view of 8.4×8.4 mm^2, corresponding to a resolution of 4.1 μm/pixel. The depth-of-field of this microscopic lens was measured to be approximately ±1 mm, allowing particles within it to be sharply focused. For both arrangements, the position and height of the imaging system were adjusted to ensure the point of impact was aligned with the centre of each image and to allow enough number of rebound particles to be recorded. One hundred shadow image pairs were collected for each case.

2.4. Particle flow conditions

Table 1 presents all particle flow conditions for the PIV measurement. Here the naming for each case incorporates the particle drop height, H, and the width of the hopper aperture, A, in the z direction. For example, H270A1.5 corresponds to the case with a free fall height of 270 mm and the hopper with an aperture of 1.5×2 mm^2, noting that the other dimension of the aperture, Δy, was kept as constant at 2 mm for all hoppers. The impact angle was varied from 75° to 15° in steps of 15° for the cases H270A1.5, H270A2.0 and H270A2.5. It is worth noting that a constant Δy led to a similar curtain thickness in the PIV imaging plane, although the variations in Δz changed the particle volume fraction on the plane because of the different influences of curtain expansion on the particle volume fraction inside the curtain. The case H270A5.0 was only tested for the impact angle of 45° to generate high volume loadings, while the case H550A2.5 achieves higher velocity with similar particle volume fractions to H270A1.5. The particle mass flow rate was measured for each run using a fast response weight-loss scale, as shown in Table 1, as is needed to determine the mean volume fraction.

2.5. Impact of individual particles

Using the same Carbo CP particle and stainless-steel plate, the impact of individual particles falling onto inclined surfaces was measured for the same series of impact angles at a constant impact velocity of 2.3 m/s. These measurements were conducted at The University of Naples by means of the experimental apparatus described elsewhere [24], here briefly reported. The apparatus consists of two Pyrex tubes, with the smaller tube been connected coaxially at the top of the larger tube to allow particles to be fed by a Pasteur pipette. Although air can be fed sideways at the top of the tube to tune particle velocity, no airflow was used in the test so that particles underwent free drop motion and reached their terminal velocity of approximately 2.3 m/s inside the tube. The stainless-steel plate was mounted 0.05 m below the bottom of the large tube, with its inclination angle been adjusted from 15° to 75° to match the desired impact angle. Single particle impact events were recorded with a progressive scan CCD camera (Photron Ultima APX) fitted with a 150-mm magnifying zoom lens and a 27.5-mm extension tube. A halogen lamp (Osram, 800 W) was used to achieve proper lighting of the impact zone. Images were collected with a sampling rate of 2000 fps and a shutter time of 42 μs. The size of the imaging window was 28×28 mm^2 (1024×1024 square pixels), corresponding to a spatial resolution of about 27 μm/pixel. Particle impact and rebound velocities, together with rebound angles, were then obtained by post-processing each recorded frame to determine the coefficient of restitution.

3. Data processing

3.1. Mean curtain thickness

Inspired by previous measurement of dispersions in particle-laden jets [25], the thickness of the particle curtain in the y-direction was derived from the planar images of laser scattering used for the PIV measurements, also termed nephelometry [26,27]. The particle scattering intensity is approximately proportional to the number of particles in a measurement volume, given that particles have a relatively narrow size distribution whilst the laser has a relative constant power (see the symmetric signal distribution in Fig. 2a) [28], and hence also scales with the local volume fraction. However, turbulent fluctuations mean that the instantaneous 'edge' fluctuates with both time and space. For this reason, the mean curtain thickness was derived from the time-averaged nephelometry images. To increase the signal-to-noise ratio, particularly for the cases with low particle loadings, scattering images were also averaged in the x-direction.

Fig. 2 presents an example of the normalised particle nephelometry intensity profile in the y-direction and the corresponding mean image from which the profile was derived. This profile was averaged from 150 laser pulses, which is sufficient to obtain convergence, while the intensity profile was measured over a height of $60d_p$ in the x-direction upstream from the point of impact as shown in the figure. The intensity profile was firstly normalised to its peak value and then fitted to a first-order Gaussian profile with a mean value of μ and deviation of σ, namely $y/\Delta_y = \mu \pm 2\sigma$ with 95% possibility. Therefore, the mean curtain thickness was defined as 4σ with two edges at $\mu \pm 2\sigma$ and termed as $\Delta_{2\sigma,y}$. The spreading angle of these curtains at height of $60d_p$ is about 0.6° based on our previous study of a free-falling curtain released from a hopper with the aperture size of 2×40 mm^2 [29]. This is sufficiently small for the spread of the curtain to be neglected for the measurement of thickness. The thickness and edge locations determined with this method were then superimposed on the particle nephelometry images as shown in Fig. 2b.

3.2. Mean particle volume fraction

The mean volume fraction of impacting particles ($\overline{\phi}$) in the curtain cross section close to the target surface was obtained from the following equation:

$$\overline{\phi} = \frac{\dot{\forall}_p}{\dot{\forall}_f} = \frac{\dot{m}_{p,i}}{\rho_p \Delta_{2\sigma,y} \Delta_{2\sigma,z} U_{p,i}} \tag{1}$$

where $\dot{\forall}_p$ (m^3/s) is the volume flow rate of particles, as measured directly from the particle mass flow rate $\dot{m}_{p,i}$ (kg/s) and density ρ_p (kg/m^3), while $\dot{\forall}_f$ (m^3/s) is the volumetric rate in the curtain, which can be deduced from the particle velocity $U_{p,i}$ (m/s) and the cross-section of the curtain

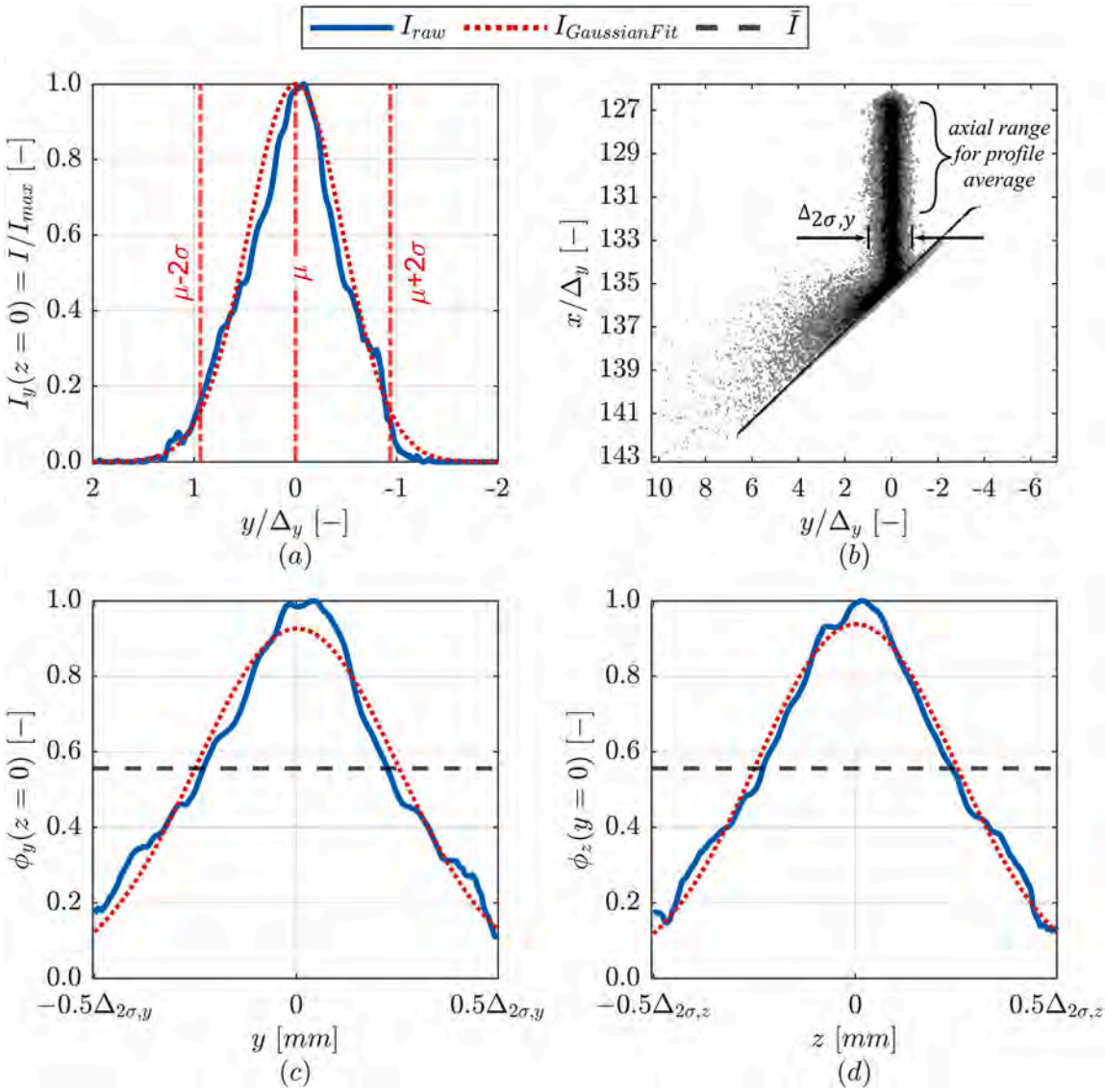

Fig. 2. (a) Normalised profile of particle nephelometry intensity, showing the centre and edges of the curtain as defined by two standard deviations from a Gaussian profile; (b) the time-averaged image obtained from 150 image together with the axial extent over which the profile was averaged and the thickness of the curtain, $\Delta_{2\sigma,y}$; (c) volume fraction distributions with (the flat dashed line) and without being spatially-averaged over the thickness at the *x*-*y* plane, as $\phi_y(z=0) = c \bullet I_y(z=0)$ and $\overline{\phi} = c \bullet \bar{I}$, where *c* is a constant; and (d) those at the *x*-*z* plane. The data are for the case H270A2.0 (Table 1).

on the *y*-*z* plane ($\Delta_{2\sigma,y} \times \Delta_{2\sigma,z}$, unit: m^2) with the assumption that the air and particles have the same velocity. The measurement of $\Delta_{2\sigma,z}$ was obtained with same process as used for $\Delta_{2\sigma,y}$ described above.

The spatial distribution of particle volume fraction was also estimated from the mean value of $\overline{\phi}$, by correcting for the distribution of the nephelometry signal intensity in the *y*-*z* plane. The normalised intensity profiles, i.e., $I_y(z = 0)$ and $I_z(y = 0)$, were used to construct a two-dimensional intensity profile $I(y, z) = I_y(z = 0) \bullet I_z(y = 0)$. This was converted into a distribution of particle volume fractions, $\phi(y, z)$, through a constant coefficient *c*, i.e., that $\phi(y, z) = c \bullet I(y, z)$, which ensures that the mean value of $\phi(y, z)$ averaged over the $[y, z] = [(-0.5\Delta_{2\sigma,y} + 0.5\Delta_{2\sigma,y}), (-0.5\Delta_{2\sigma,z} + 0.5\Delta_{2\sigma,z})]$ equals to the $\overline{\phi}$ value obtained above from Eq. 1. The root mean square (RMS) values of $I_y(z{=}0)$ and $I_z(y{=}0)$ were also obtained from 150 scattering images and converted to the RMS of $\phi_y(z{=}0)$ and $\phi_z(y{=}0)$, respectively, by multiplying the coefficient of *c*. Fig. 2c and d present the profiles of scattering signals with and without being spatially-averaged over the curtain thickness, for the *x*-*y* plane and *x*-*z* plane, respectively.

3.3. In-plane rebound ratio of particles

Impacting particles either rebounded from, or slid/rolled along, the target surface. As shown in Fig. 1d, the particles also rebound within a range of angles bounded by the angle β. However, only the particles rebounding within the laser sheet, that is in the *x*-*y* plane, can be accessed from the planar scattering images. Those rebounding out of this plane are not captured with this measurement. Therefore, the in-plane rebound ratio of particles ($K_{\delta LS}$) was estimated. The method is explained as follows:

1) The in-plane rebound ratio $K_{\delta LS}$ is expressed as:

$$K_{\delta LS} = \frac{\dot{m}_{p,r,\delta_{LS}}}{\dot{m}_{p,i,\delta_{LS}}} \tag{2}$$

where $\dot{m}_{p,r,\delta_{LS}}$ and $\dot{m}_{p,i,\delta_{LS}}$ are the mass flow rates (kg/s) of rebounding and impacting particles in the *x*-*y* plane, respectively.

The mass flow rate of the particles within the laser sheet in *x*-*y* plane can be calculated:

$$\dot{m}_{p,i,\delta_{LS}} = \int_0^{\Delta_{2\sigma,y}} n_{p,i}(x,y)\cdot U_{p,i}(x,y)\cdot M_p\cdot dy \tag{3}$$

where $n_{p,i}$ is particle number density of impacting particles, $U_{p,i}$ (m/s) is particle impacting velocity, M_p (kg) is the mean particle mass, and $\Delta_{2\sigma,y}$ (m) is the mean curtain thickness in the y direction. The particles rebound within an angle of Θ from 0 to π, so that the mass flow rate for all rebounding particles within the laser sheet can be calculated by:

$$\dot{m}_{p,r,\delta_{LS}} = \int_0^{\pi} n_{p,r}(x,y)\cdot V_{p,r}(x,y)\cdot M_p\cdot r\cdot d\Theta \tag{4}$$

where r (m) is the radial distance of rebounding particles to the impacting location O'. Then, the rebound ratio $K_{\delta LS}$ in the x-y plane can be calculated theoretically by:

$$K_{\delta LS} = \frac{\int_0^{\pi} n_{p,r}(x,y)\cdot V_{p,r}(x,y)\cdot r\cdot d\Theta}{\int_0^{\Delta_{2\sigma,y}} n_{p,i}(x,y)\cdot U_{p,i}(x,y)\cdot dy} \tag{5}$$

2) Given the narrow distribution of the particle size and the uniform laser flux in the x- direction, the particle number density can be estimated from the nephelometry signals, and the integration in Eq. 5 can be represented by the nephelometry signals accumulated within two corresponding areas, i.e., one at the incoming particle region and the other at particle rebounding region. Therefore, the value of $K_{\delta LS}$ was evaluated from the measured scattering images with the following processes.
3) Referring to Fig. 3, Region-I represents the inflowing particles with a propagation path of Δx_I, also assuming that this region is far enough upstream to avoid non-negligible influence from bouncing particles. The length of the rebounding region within which particles are counted, Region-II, is related to that of the input flow by correcting for their different velocities, as follows $\Delta x_I / |U_{p,i}| = \Delta x_{II} / |V_{p,r}|$. The value of $\Delta x_I = 40d_p$ was chosen for all cases as providing the most reliable measurements.
4) As part of Region-II, Region-IIb (Fig. 3), which is the mixed inflow and rebound region, consists of both incoming and rebounding particles. A signal correction process was therefore applied to deduct incoming particles, by subtracting the accumulated signals in the signal correction region, Region-IIa, which is the close upstream of Region-IIb with the same length as Region II (i.e., $\Delta x_{IIa} = \Delta x_{II}$) that contains no rebounding particles, from the accumulated nephelometry signals within Region-II.
5) Then the value of $K_{\delta LS}$ can be evaluated through the scattering signal intensity, expressed as $K_{\delta LS} = (S_{II} - S_{IIa}) / S_I$, where S is the sum of the nephelometry signal intensity within each region.

3.4. PIV analysis for particle velocity

PIV images were processed to obtain particle velocities, from which statistical results of the particle impact and rebound velocities, together with the rebound angle, were obtained. The open-source software PIVlab (version 2.53) was used to process the PIV image pairs. The multi-pass approach with two interrogation window sizes, 256×256 pixels and 128×128 pixels, was selected based on the particle size on the image (~10 pixels) to ensure enough particles were included within the window, together with an overlap of 50%. Post processing was also applied to remove noise by the functions 'select velocity limit' and 'filter low contrast threshold', which are available in the PIVlab software. Particle velocity vectors were extracted from the PIV results for statistical analysis. Based on the direction of velocity vectors, particles were categorised as impacting or rebounding, following which probability distribution functions (PDFs) were calculated for the speed and rebound angle.

The accuracy of the PIV measurements was assessed by analysing the mismatch of centroids of particle pairs in each interrogation window for an image pair [30]. This was achieved by four steps. The first was to obtain the coordinates of particle centroids in each interrogation window from subsequent frames (namely frame A and B, respectively). Then centroids of frame A were translated by pixel values converted from velocity vectors of corresponding interrogation windows to obtain coordinates of particle centroids of the translated frame (namely frame A_T). After this, the mismatch, or disparity D, of centroids of particle pairs in each interrogation window was obtained from the following equation:

$$D = (D_x, D_y) = (x_{A_T} - x_B, y_{A_T} - y_B) \tag{6}$$

where D_x and D_y are disparities in the x and y direction, respectively, x_{A_T}, x_B, y_{A_T} and y_B are coordinates of particle centroids of frame A_T and frame B, respectively. Finally, Gaussian distributions were obtained

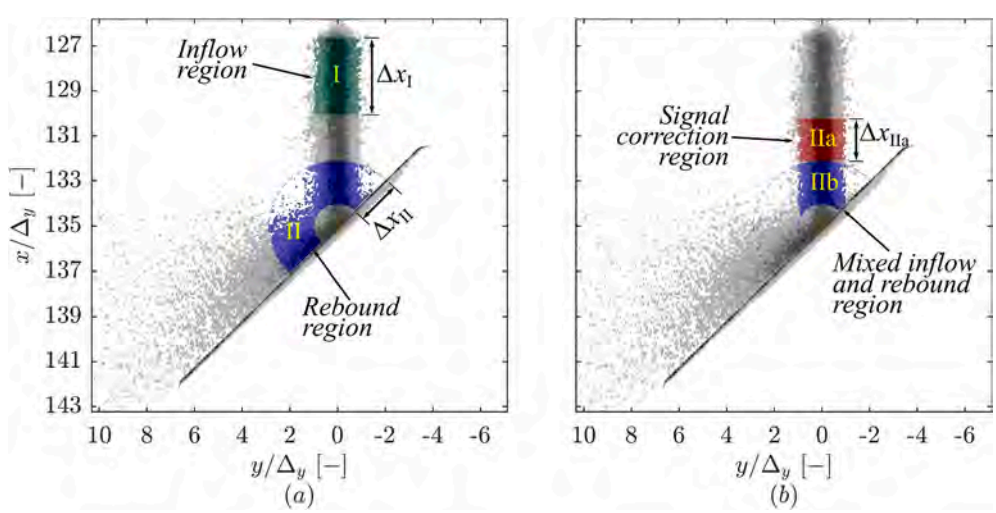

Fig. 3. Characterisation of the in-plane particle rebound ratio from the mean nephelometry image, showing (a) the inflow region, Region I, which represents the incoming particles (green) with a propagation path of $\Delta x_1 = 40\ d_p$, and the rebound region, Region II, used to count the rebounding particles (blue), with length $\Delta x_{II} = |V_{p,r}| / |Up,i| \cdot \Delta x_I$, where $|U_{p,i}|$ and $|V_{p,r}|$ are magnitudes of particle mean impact and rebound velocities, or speeds; and (b) the signal correction region, Region IIa, used to deduct incoming particles from the mixed inflow and rebound region, Region IIb, by subtracting the sum of nephelometry signals within Region IIa (red) from that within Region II. (For interpretation of the references to colour in this figure legend, the reader is referred to the web version of this article.)

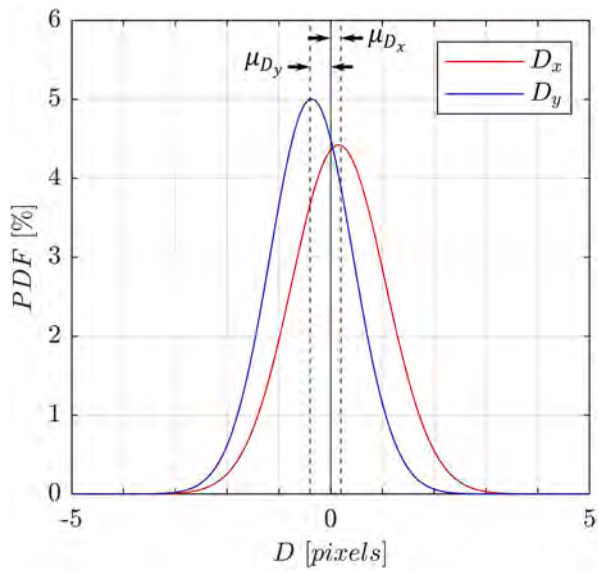

Fig. 4. Distributions of the disparity vectors (see Eq. 6), whose mean values show the mismatch of particle pairs on an image pair for both x and y directions.

from the histogram of the disparity vector components, which were used to analyse the accuracy.

Fig. 4 presents distributions of the disparity vectors of a randomly selected image pair, which contains about 100 valid particle centroids. The figure reveals that the mismatch of particle pairs during the cross-correlation process is $\mu_{D_x} \approx 0.2$ pixels in x direction, while $\mu_{D_y} \approx 0.5$ pixels in y direction. The typical displacement of impacting particles during the time interval is about 27 pixels, therefore, the uncertainty in the PIV measurements are approximately 0.7% and 1.9%, respectively.

4. Results and discussion

Figs. 5a – 5e present a series of single-shot images recorded at the five different impact angles for the case H270A2.0. As can be seen, rebounding particles span a wide range of angles in the x-y plane, particularly at large impact angles, such as those shown in Fig. 5a for $\alpha = 75°$. The spread width of rebound angles decreases with the impact angle because of the decrease in the normal component of particle velocities with the impact angle, corresponding to reduced repulse energy [15]. Figs. 5f – 5j present the corresponding time-averaged particle scattering images, each comprising the superposition of 150 successive single-shot images. The results reveal a decrease in the spread width of rebound angles with the impact angle, consistent with single-shot images.

The time-averaged images also show that there is a higher particle concentration in the region close to the point of impact compared with

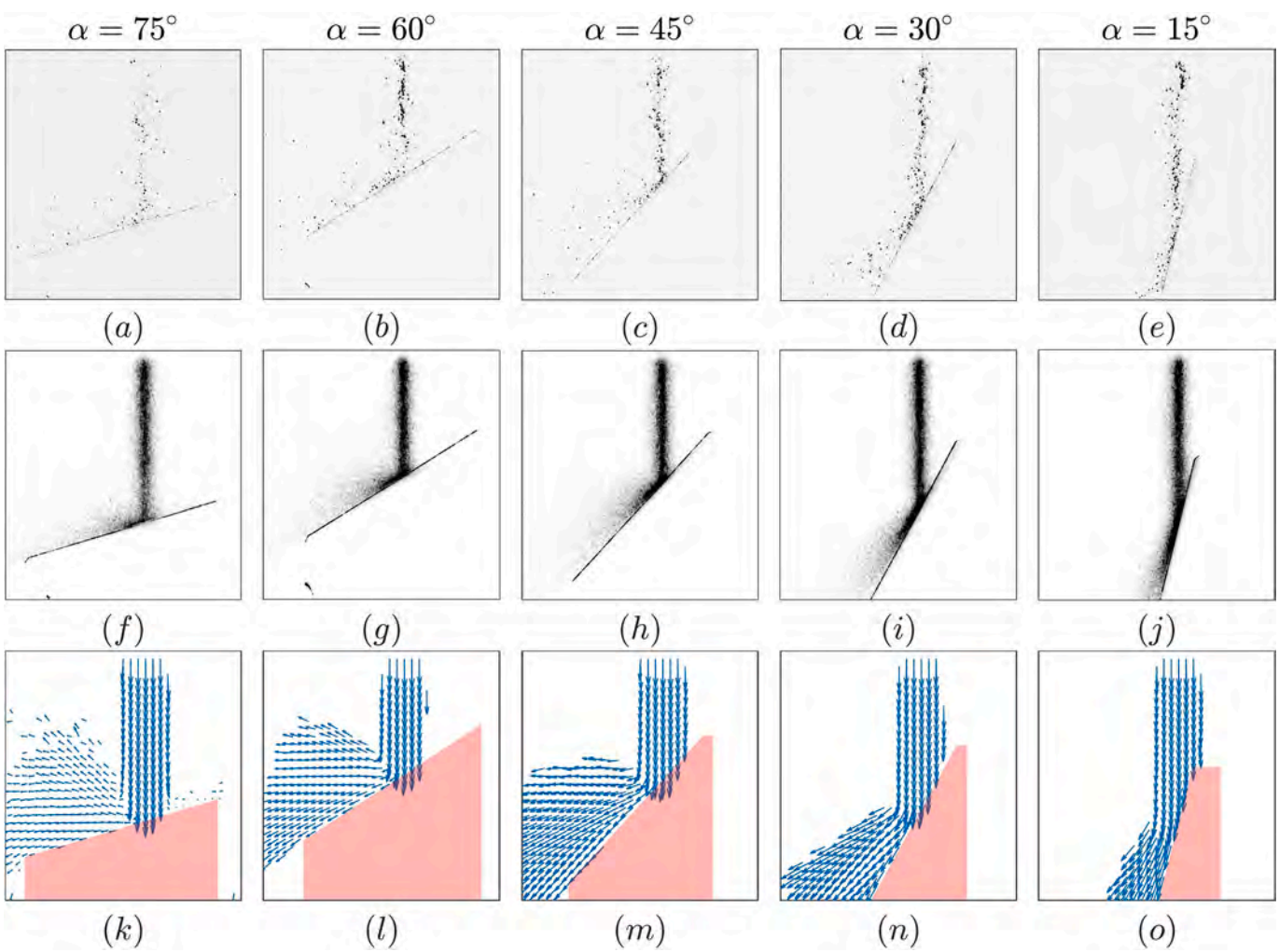

Fig. 5. Representative cases of single-shot (a – e), superpositions of 150 successive images (f – j), and particle velocity vectors averaged from 150 successive images (k – o) for a series of impact angles. Particle flow condition is H270A2.0 (see Table 1).

Table 2
Measured values of curtain thicknesses and mean particle volume fractions as measured just upstream from the inclined plate for the experimental cases shown in Table 1.

Cases	$\Delta_{2\sigma,y}$ [mm]	$\Delta_{2\sigma,z}$ [mm]	$\overline{\phi}$ [%]
H270A1.5	4.09	3.68	0.24
H270A2.0	3.75	3.82	0.41
H270A2.5	3.20	2.73	1.09
H270A5.0	3.07	4.43	2.40
H550A2.5	5.45	5.66	0.22

that in the incoming flow, which is attributed to the formation of a particle layer in this near wall region. The number of particles in this region increases with a decrease in the impact angle (from Figs. 5f to 5j), resulting in different wall boundary conditions which in turn affect the behaviour of rebounding particles. For example, at small impact angles, e.g. Fig. 5j, the particle layer tends to flow down the inclined surface as a chute flow that causes particles to slide or rebound in the direction along the inclined surface. Rebounding particles bounce to different directions, not limited in the *x*-*y* plane, and the scattering signals decrease compared to that before impact. Figs. 5k – 5o present the corresponding particle velocities for the series of images shown in Figs. 5f – 5j, which were averaged over 150 image pairs. In addition to consistently revealing that rebounding particles span broad directions at high impact angles, Figs. 5k – 5o show that the magnitudes of rebound velocity (rebound speed) of particles increases with the decrease in impact angle, indicating lower energy loss during the impact on the wall.

Table 2 presents measurements of the curtain thickness and mean particle volume fractions of the particles measured just upstream from the target surface. This shows that this range of hopper exit dimensions and fall heights can be used to generate particle volume fraction ($\overline{\phi}$) that vary by an order of magnitude and a wide range of path lengths normal to the plate, $\Delta_{2\sigma,y}$. Furthermore, $\overline{\phi} > 0.1\%$ for all cases, which means that all of these particle-laden flows are within the four-way coupling regime. The trends are also consistent with previous work. For example, an increase in aperture width for a constant dropping height of $x = 270$ mm leads to an increase in $\overline{\phi}$, which is consistent with the previous finding that an increase in mass flow rate decreases the dispersion rate of the curtain due to the decreased rate of air entrainment [31]. The air entrainment also increases with the fall height, leading to the increased thickness at H550A2.5 [32]. No trend was observed for $\Delta_{2\sigma,z}$, because the hopper widths and the initial thicknesses of curtain are different for these cases.

Fig. 6 presents the profiles of locally averaged values of ϕ in the *y* and *z* directions for all the experimental cases listed in Table 2, together with the corresponding distributions of RMS. It can be seen that the profiles for the highest loading, with a value at the centre of $\phi \approx 4.5\%$ for the case H270A5.0, have a Λ shaped distribution, while those with lower loadings approach a Gaussian distribution. In addition, whilst the peak concentration in the former cases approaches to the dilute regime of granular flows ($10\% < \phi < 50\%$ [33]), all cases are within the four-way coupling regime of particle laden-flows ($\phi > 0.1\%$ [18]).

The distributions of RMS normalised by corresponding mean value are approximately uniform and low on the axis, with fluctuation of <2% there, peaking toward the edge. This is consistent with previous measurements of particle-laden jets in the two-way coupling regime [26,27] although, to the best of our knowledge, analogous measurements in the four-way coupled regime are yet to be reported. It is consistent with the role of the shear-layer generating large-scale unsteadiness in the instantaneous distributions. The good collapse of all profiles also confirms that all are in the same four-way-coupled regime. Similar profiles and magnitudes of particle volume fractions can also be observed for cases H270A1.5 and H550A2.5 but with different velocities (see Fig. 11).

Fig. 7a presents the in-plane particle rebound ratios measured for a series of values of impact angle and mean particle volume fraction. The in-plane rebound ratio, which is the fraction of particles that do rebound from the wall, is always less than unity and increases with a decrease in the impact angle. That $K_{\delta_{LS}} < 0.7$ shows that at least 30% of the particles do not rebound, but rather form a layer adjacent to the surface. That $K_{\delta_{LS}}$ decreases as the impact angle approaches the normal direction is contrary to what would be expected for a single particle with an inelastic collision. That is, for a single particle, the component of rebound normal to the wall will increase as the impact angle approaches 90°.

Fig. 7b presents the influence of the impact angle and mean particle volume fraction on the lateral dispersion of rebounding particles. It shows an increase in dispersion angle, corresponding to an increase in the number of out-of-plane particles, with a decrease in impact angle. This provides a mitigating explanation to the increase of $K_{\delta_{LS}}$ as the impact angle decreases, namely that more particles rebound out of the laser sheet with an increase in impact angle, leading to fewer particles being detected within the imaging plane.

Fig. 8 presents PDFs of particle impact and rebound velocities, together with the rebound angle and the coefficient of restitution, measured for a series of particle loadings at a constant impact angle of 45°. In addition, the mean values ($\overline{U}_{p,i}$, $|\overline{V}_{p,r}|$, $\overline{\Theta}$ and $\overline{e}$) and distribution range (σ) of the results are also presented, with the latter defined as the range within which 68.4% of the values are distributed (even for a non-Gaussian profile). Fig. 8a and b show that the mean value of the impact velocity increases with the particle volume fraction, which is consistent with understanding that dense particles distributions reduce the drag force acting on particles within the curtain [32]. The impact velocity also approaches the maximum expected velocity of free-falling particles at the measured drop height, which was calculated to be $U_{limit} = (2gH)^{0.5} = 2.3$ m/s as the case in which particles have no drag [6]. The mean value of the distribution range decreases with an increase in the particle volume fraction. This can also be explained by the reduction of curtain thickness (Table 2) and drag coefficient resulting in the particles having a similar velocity across the curtain [32].

Fig. 8c and d present the measured values of particle rebound speeds measured for a series of particle loading. They show that the mean values of particle rebound speed increase initially, but then remain approximately constant with an increase in the particle volume fraction. This is attributed to two combined and competing influences. On the one hand, an increase in ϕ causes an increase in particle impact velocity (Fig. 8a and b), while, on the other, it also causes an increase in the thickness of the particle surface layer (see Fig. 7a), leading to increased energy dissipation via inelastic rebound that tends to reduce rebound speed. The distribution range of rebound speed also decreases as particle volume fraction increases, revealing less velocity variation for rebounding particles. This reduced variability in the rebound can be explained by the reduction in the rebound angle, presented next.

Fig. 8e and f present the result of particle rebound angles, showing that the mean particle rebound angle decreases as the mean particle volume fraction is increased. This suggests that the sliding particles transfer some momentum to the rebounding particles in the direction of the surface, increasing the relative velocity in this direction. A potential additional influence is the increased probability for rebounding particles to collide with impacting particles due to the increased particle volume fraction and decreased curtain thickness at high particle loading, as presented in Table 2. Furthermore, the increased influence of the sliding particle layer at higher particle volume fractions also acts to reduce the mean value and variations of rebound angles (Fig. 8d).

Fig. 8g and h present relationship between coefficient of restitution, $e = |V_{p,r}|/|\overline{U}_{p,i}|$, and the mean particle volume fractions. The mean values of *e* are approximately 0.57 for all measured cases, which implies a weak dependence on particle loading. The significant reduction relative to the values for individual particles is attributed to the influence of the surface layer. This near independence of the value of e from ϕ is attributed to the simultaneous increase of both particle impact and

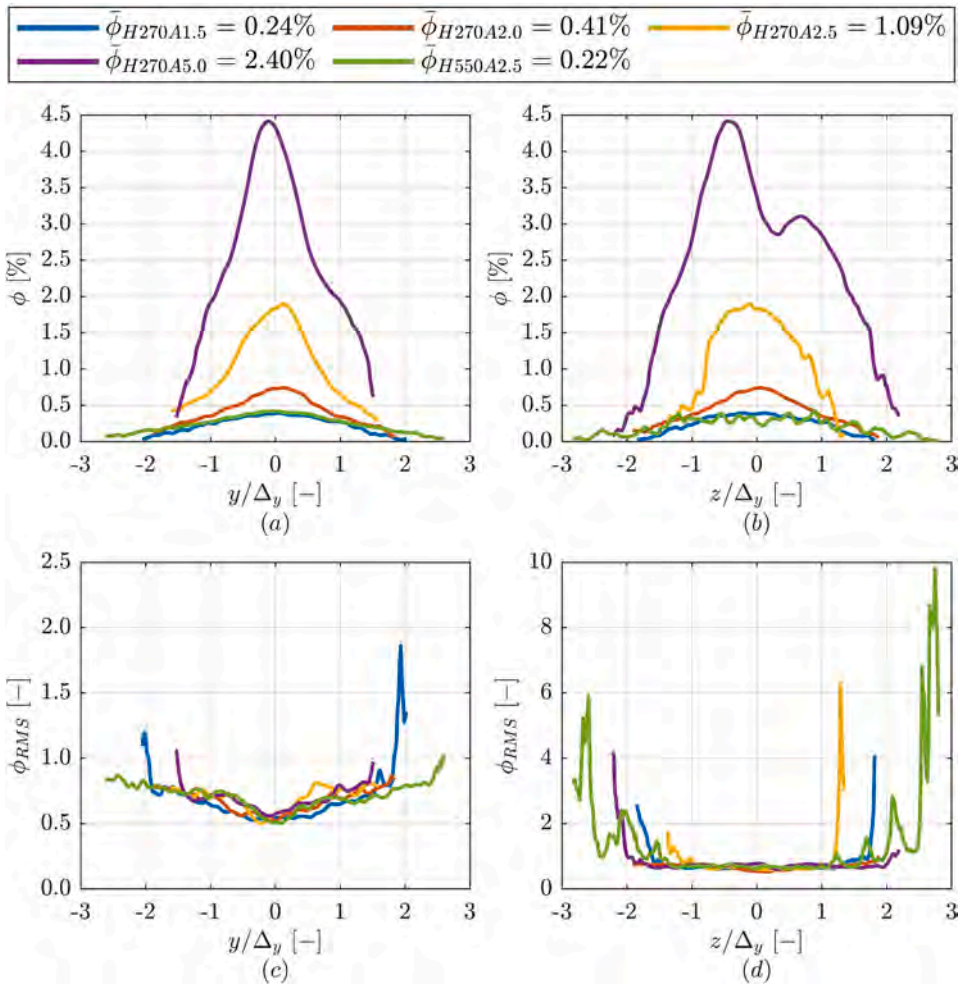

Fig. 6. The distributions of (a) and (b): the mean particle volume fraction in the y and z directions, respectively, and of (c) and (d) of the normalised root mean square (RMS) variations of particle volume fractions in the y and z directions, respectively. Other experimental conditions are shown in Table 2.

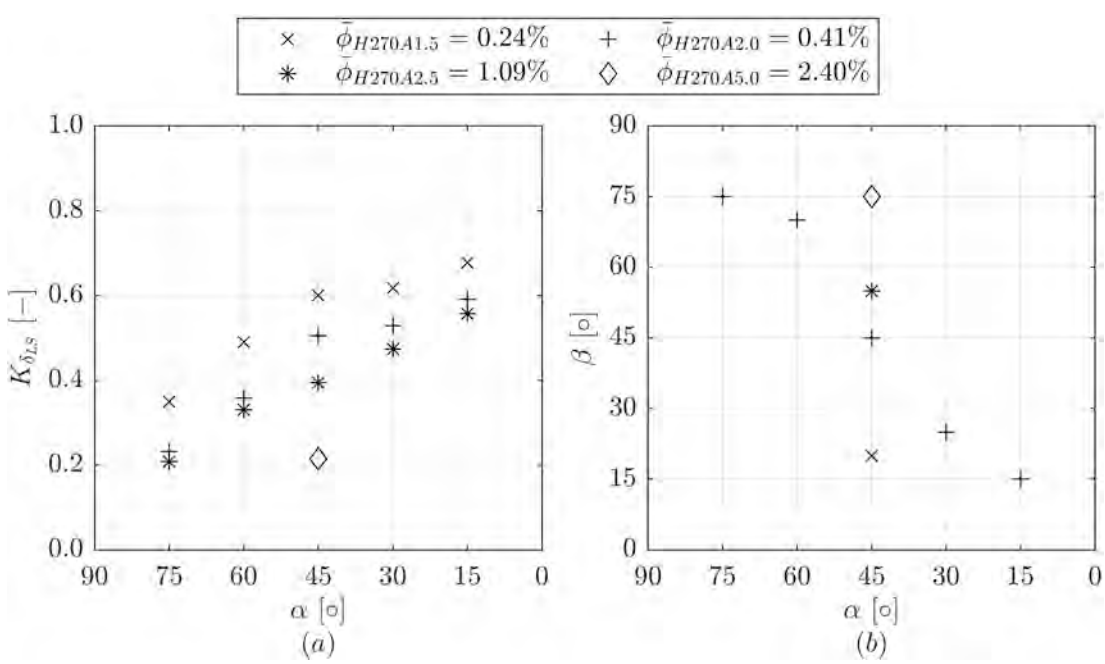

Fig. 7. Effect of varying impact angles, α, on (a): in-plane rebound ratio of particles, $K_{\delta_{LS}}$, and, (b): particle dispersion angle, β, of the entire curtain at a series of values of mean particle volume fraction, $\bar{\phi}$.

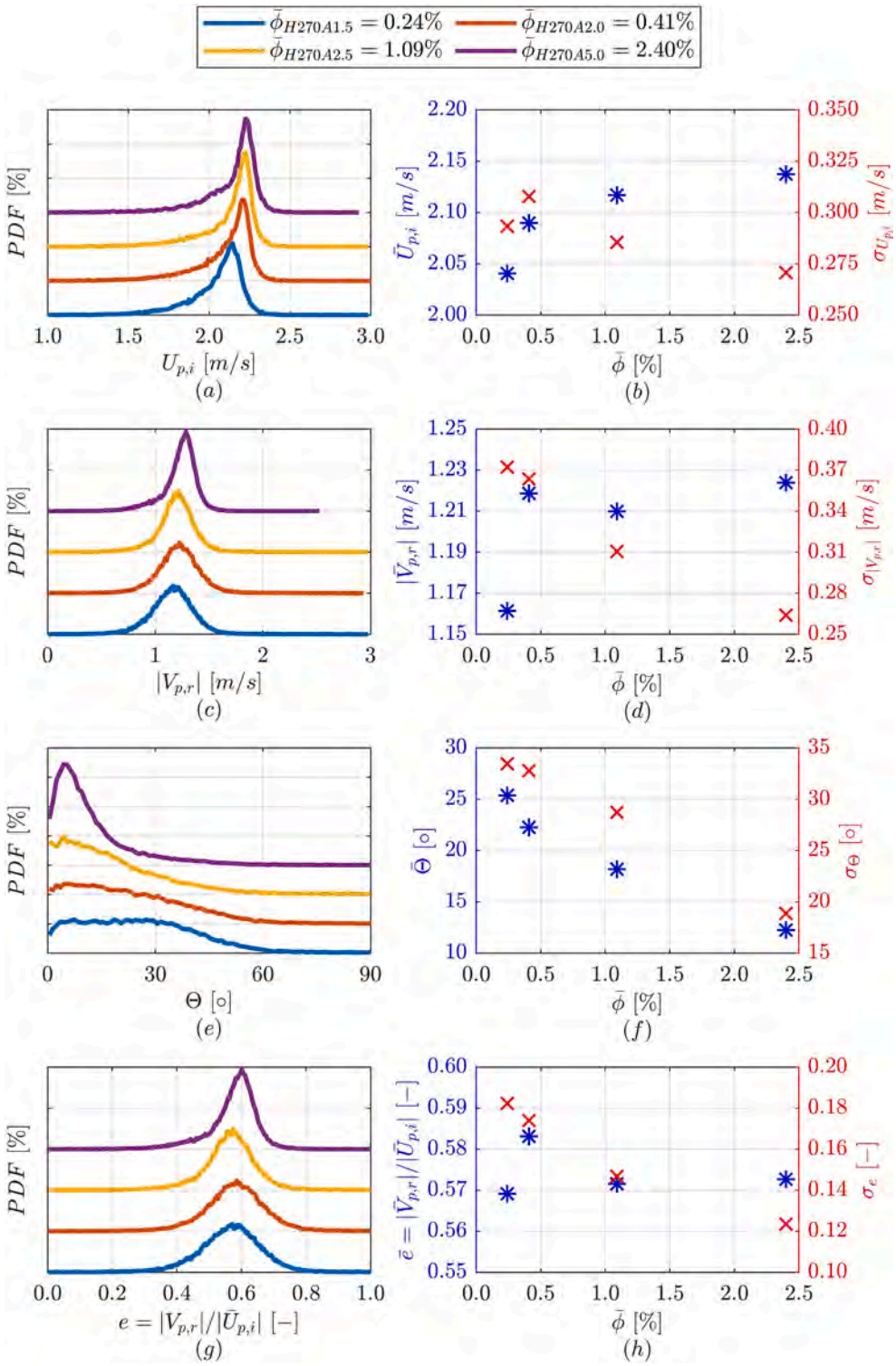

Fig. 8. Probability density distributions of particle impact velocity ($U_{p,i}$), rebound speed, ($|V_{p,r}|$), rebound angle (Θ) and coefficient of restitution (e) for a series of flow conditions at a constant impact angle of $\alpha = 45°$. The mean values ($\overline{U}_{p,i}$, $|\overline{V}_{p,r}|$, $\overline{\Theta}$ and $\overline{e}$) are shown in the right column, with the distribution ranges (σ is defined as the range within which 68.4% of the values are distributed) are shown on the secondary axis.

rebound velocities with it (Figs. 8a to 8d). The distribution range of e decreases with the mean particle volume fraction, which is consistent with that of rebound speed.

Fig. 9a and b present the mean and instantaneous shadow image distributions of particles after impact for the input condition H270A2.0 and an impact angle of $\alpha = 45°$. A wide spread can be seen in the distributions of particles after impact, revealing a wide range of rebound directions, which is consistent to Fig. 8e and f. Fig. 9a and b also reveal the presence of a layer adjacent to the surface close to the point of impact, as deduced above, while Fig. 9a confirms that the layer is moving along the surface, implying a sliding particle layer/chute flow. The chute flow can be observed to consist of approximately 2–3 layers of particles in Fig. 9a, depending on whether the velocity vector is parallel to the plate.

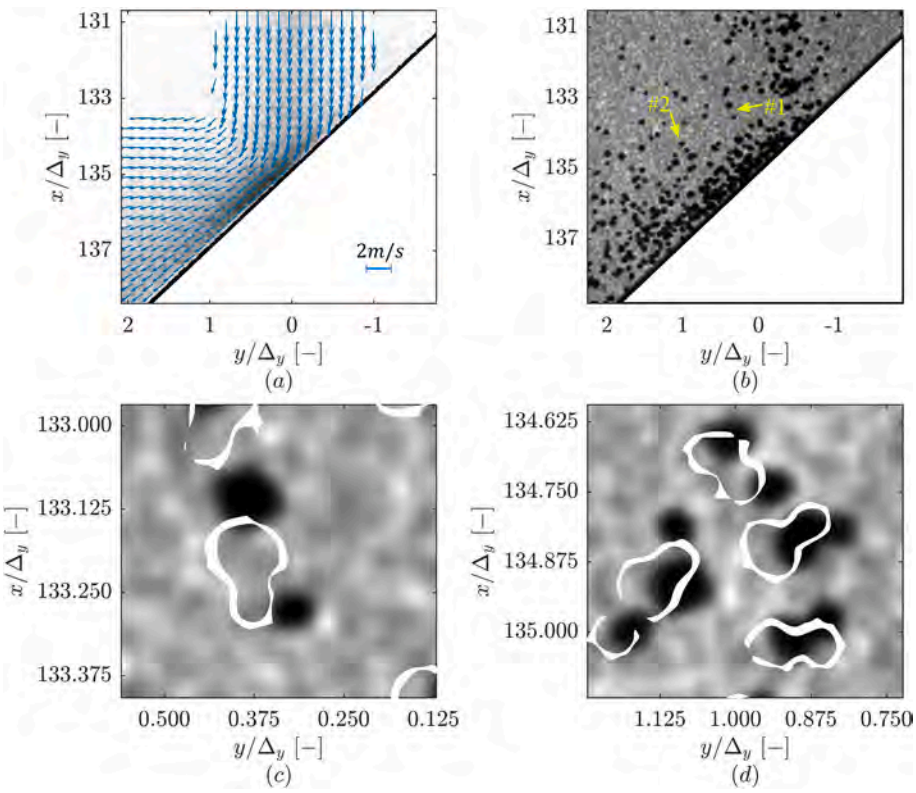

Fig. 9. Representative images of impacting and rebounding particle flows for the case of H270A2.0 at $\alpha = 45°$ (a): the mean shadowgraph with measured mean particle velocity vectors; (b) the instantaneous shadowgraph with inter-particle collisions labelled with yellow arrows; (c): a selected zoomed-in instantaneous shadowgraph of collision #1 from (b) with the detected edges of particles from the subsequent PIV image frame to show particle displacements; and (d) the corresponding case for collision #2. (For interpretation of the references to colour in this figure legend, the reader is referred to the web version of this article.)

Also highlighted in Fig. 9b are specific cases where collisions occur between incoming and rebounding particles, which are highlighted in yellow and numbered (labels #1 and #2). Zoomed-in images of the two specific cases are shown in Fig. 9c and d, with edges of these particles in the second frame highlighted to reveal their displacements. These particles were identified as corresponding to such a collision from their displacements. For example, the vertical and horizontal displacements in Fig. 9c indicate that the large and small particles are incoming and rebounding particles, respectively, while the overlap of their edges reveals the occurrence of collision. Since the number of collisions between incoming and rebounding particles is modest, and because previous report has shown that particle-particle interactions play a minor role in particle-laden flows with particle volume fractions of <0.1 [33] while the maximum particle volume fraction in the present work is 0.045 (occurring for the case H270A5.0), the influence of inter-particle collisions on rebound behaviour is deduced to be secondary compared to that of the particle layer.

Fig. 10 presents PDFs of impact and rebound velocities, together with rebound angle and coefficient of restitution, for the case H270A2.0 at a series of impact angles, together with the mean and distribution range of the data. The mean values of impact velocity shown in Fig. 10b reveal that the input flow to the experiment is repeatable to within 1.3%. The particle rebound speed decreases approximately linearly as the impact becomes more normal (i.e. with an increase in the impact angle), which also results in a linear decrease of e (Fig. 10h). The trend of rebound speed/coefficient of restitution contrasts those of previous measurements for single particles, which decreases first then becomes almost constant as the plate angle moves to the normal direction [34]. This difference can be explained by the formation of the sliding particle layer/chute flow (Fig. 5). Tilting the plate to be more vertical will increase the velocity of the sliding particle layer, providing a plausible explanation for the measured increase in their mean rebounding speed, thereby increasing the coefficient of restitution. Distribution ranges of both rebound speed and coefficient of restitution are less affected by the impact angle, as been revealed in Fig. 10d and h.

Fig. 10e and f present the PDFs, together with the mean value of distribution range of particle rebound angle. As shown in Fig. 10f, the mean value of particle rebound angle decreases as the impact angle increases. The trend is consistent with the explanation that the decrease in the normal component of particle velocities with the impact angle reduces the repulse energy, thereby decreasing the spread width of rebound angles (Fig. 5). Fig. 10f also shows that the distribution range of rebound angle increases with the impact angle. This can be explained by the particle layer being less likely to slide as the plate becomes more horizontal (Fig. 5), leading to a thicker surface layer that will increase the variability in the rebound. In contrast, the layer tends to slide as the plate becomes more vertical, reducing its thickness and also the variability in the rebound.

Fig. 11 compares the measured distribution of rebound angle and coefficient of restitution for two cases, H270A1.5 and H550A2.5, which have similar particle volume fraction but different curtain thickness and impact velocity, for a series of impact angles. Although curtain thickness was changed during measurements, it is considered to be a secondary influential factor comparing to impact velocity, because larger curtain thickness increases the probability of rebounding particles to collide with other particles, while the influence of inter-particle collision is deduced to be secondary compared to that of the particle layer. Therefore, impact velocity is considered to be the key factor that lead to the difference between the two cases.

Fig. 11a and b show the PDFs and the mean value of rebound angle for cases H270A1.5 and H550A2.5. They show that, at a given impact angle, the particle rebound angles are more closely distributed toward lower values as the particle velocity increases. Moreover, cases with $\overline{U}_{p,i} = 2.1$ m/s have more uniform distribution curves than cases with $\overline{U}_{p,i} =$

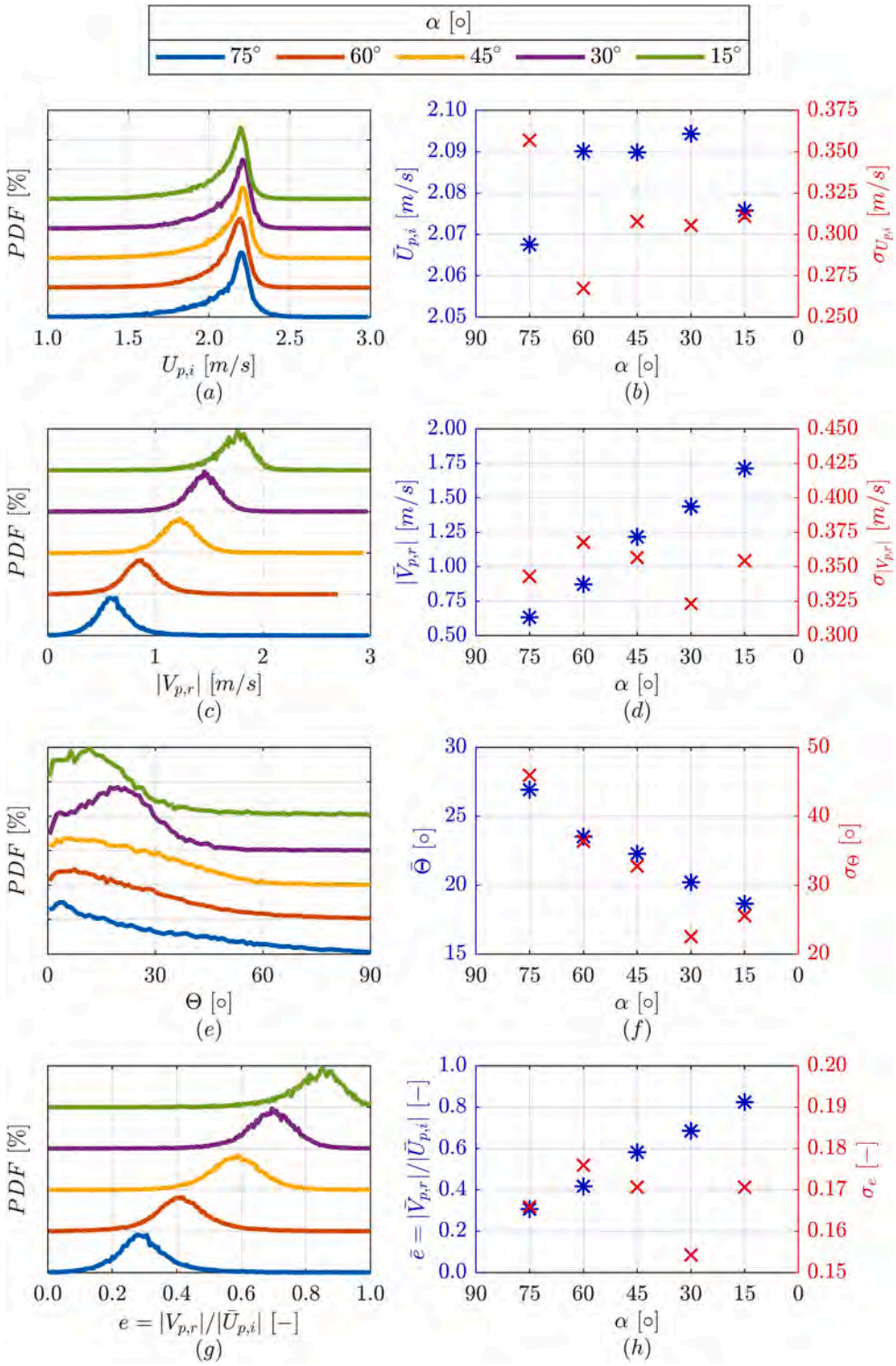

Fig. 10. Probability density distributions of particle impact velocity ($U_{p,i}$), rebound speed, ($|V_{p,r}|$), rebound angle (Θ) and coefficient of restitution (e) for a series of impact angles at a constant particle volume fraction of $\overline{\phi}_{H270A2.0} = 0.41\%$. The mean values ($\overline{U}_{p,i}$, $|\overline{V}_{p,r}|$, $\overline{\Theta}$ and $\overline{e}$) are shown in the right column, with the distribution range (σ is defined as the range within which 68.4% of the values are distributed) are shown on the secondary axis.

3.0 m/s for $\alpha > 30°$, revealing a reduction in the range of rebound directions with the increase of particle impact velocity. One potential explanation for these findings is that, the increased impact velocity increases the kinetic energy of incoming particles, since the particle layer is less likely to slide for normal impacts, large impacting velocity results in substantial particle penetrations within the layer, during which rebound will be inhibited as more energy is dissipated through successive interactions between the penetrating particle and layer particles [35]. Penetration of particles is less significant as the plate becomes more oblique due to the slide of the particle layer, resulting in less difference between the two cases for $\alpha \leq 30°$.

Fig. 11c and d show PDFs and the mean value of e for the corresponding conditions. As can be seen, the mean value of e for cases with $\overline{U}_{p,i} = 3.0$ m/s are smaller than that for cases with $\overline{U}_{p,i} = 2.1$ m/s for $\alpha \geq$

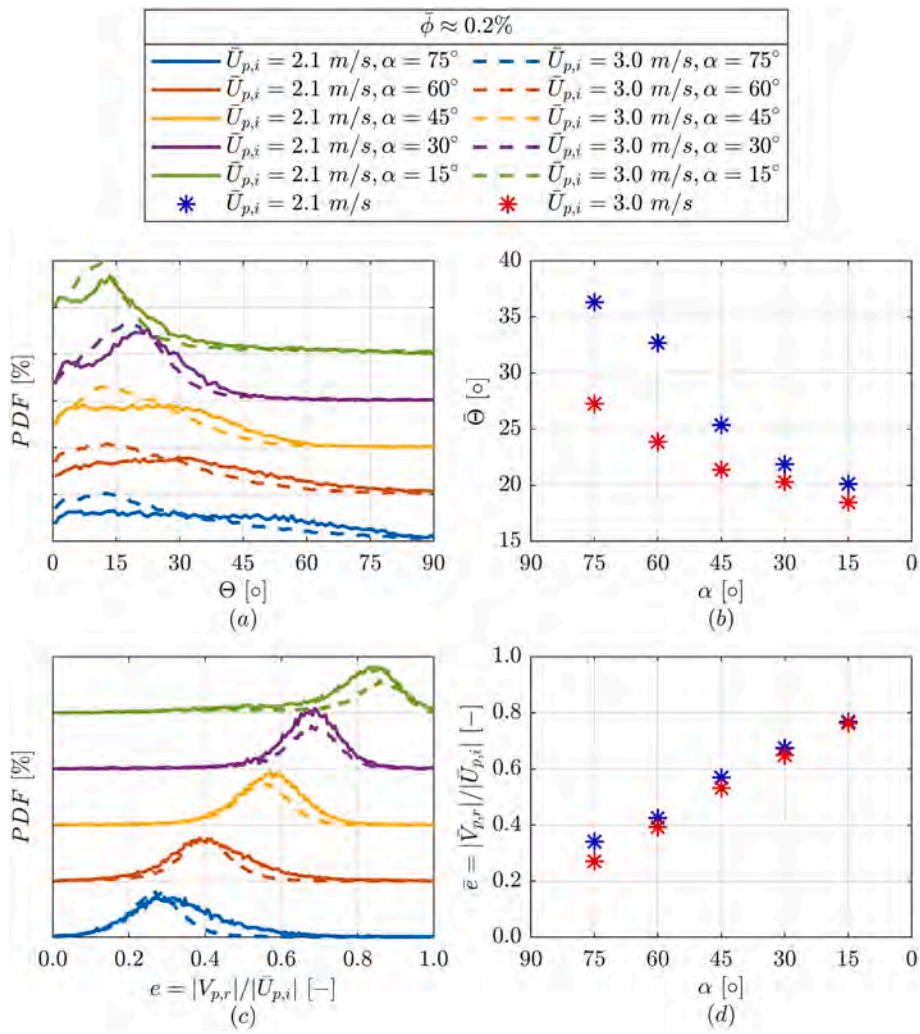

Fig. 11. Probability density distributions of rebound angles (Θ) and coefficient of restitution (e) for two mean impact velocities, $\overline{U}_{p,i}$ = 2.1 m/s and $\overline{U}_{p,i}$ = 3.0 m/s, and a series of values of impact angles at a fixed mean particle volume fraction of $\overline{\phi}\approx$ 0.2%. The mean values ($\overline{\Theta}$ and $\overline{e}$) are shown in the right column.

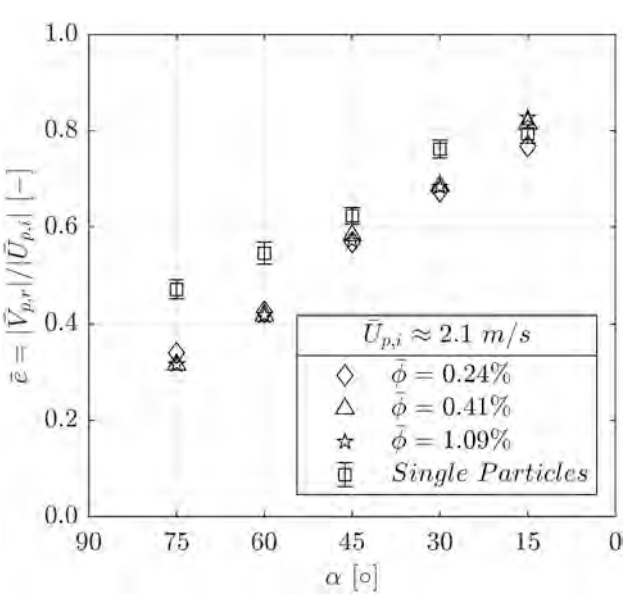

Fig. 12. Comparison of the coefficient of restitution as a function of impact angle as measured both for a series of particle-laden flows and for single particles.

30°, which is consistent with the explanation that increasing the impact velocity results in increased energy dissipation. The difference between $\overline{e}$ decreases with the impact angle, i.e. from $\Delta\overline{e}$ = 0.07 at α = 75° to <0.01 at α = 15°, which is also consistent with the statement that energy dissipation is less influential because of the sliding layer/chute flow.

Fig. 12 presents the mean values of coefficient of restitution, $\overline{e} = |\overline{V}_{p,r}|/|\overline{U}_{p,i}|$, measured from particle-laden flows with a series values of volume fractions, comprising $\overline{\phi}$ = 0.24%, 0.41% and 1.09%, and from single particles at a constant impact velocity for a series values of impact angles. As can be seen, the measured value of e increases for both particle curtains and single particles as the impact angle decreases. This is attributable to decreased energy loss with increasingly tangential impact [36]. In addition, for almost all impact angles, the value of $\overline{e}$ measured for particle-laden flows is lower than that for single particles, with the difference being greatest at the largest impact angle of α = 75° and decreasing to become small as the flow becomes more tangential. This provides further evidence, firstly, that the formation of the particle layer introduces extra energy dissipation through frictional processes within the layer and through interactions between incoming and layer particles (Figs. 8, 10 and 11 [35]), and secondly, that the transfer of momentum from sliding-layer/chute-flow becomes increasingly influential as the plate becomes more vertical, which increases particle rebound speed.

5. Conclusion

The detailed measurements and analysis of a systematic investigation of free-falling particle-laden flows impacting onto an inclined surface have yielded new insights. It was found that increasing the particle volume fraction within the four-way coupled regime acts to increase the probability that rebounding particles collide with incoming particles to inhibit their rebound. This results in the formation of a particle layer on the surface for those flows with sufficiently high particle volume fractions and for impact angles that are sufficiently close to the normal direction. The layer, where present, acts to absorb energy, reduce the rebound speed and increase the range of rebound angles for impact angles close to the normal direction, while it accelerates those impacting particles which rebound with a component in the direction of the sliding layer, to increase their rebound speed and decrease the range of rebound angles as impacts become more oblique. In addition, the tilting of the plate toward the vertical direction increases the probability that the particles slide away from the point of impact, together with the velocity, and momentum, of the sliding-layer (or chute-flow). Some of this momentum is transferred to the rebounding particles to modify the rebounding angle, making it more oblique.

The more specific results of the present work are as follows:

- The formation of a layer of particles on the surface has been confirmed to occur for volume fractions of greater than or equal to 0.41%, both by measurement of particle rebound speed and rebound angle, together with the coefficient of restitution, and by direct experimental observation.
- Increasing the particle volume fraction in the curtain for a given impact angle increases particle impact velocity, thereby increasing the particle rebound speed. It also increases the number of sliding particles within the layer, which increases the thickness of the layer, leading to increased energy dissipation that reduces the rebound speed. The sliding particle layer transfers some momentum to the impacting particles to make the rebound angle more oblique. This increases with the particle volume fraction, resulting in less variability in the rebound.
- A reduction in the angle of impact, to make it more oblique, results in an approximately linear increase in particle rebound speed. This occurs by increasing the establishment and the influence of the sliding layer/chute flow, which transfers momentum to the rebounding particles, while reducing the range of rebound angles.
- The mean coefficient of restitution, $\bar{e}$, measured for single particles with large impact angles is larger than that for particle-laden flows of sufficiently high volume fraction. This can be explained by the observed formation of the particle layer, which increases energy dissipations through frictional processes. However, the increase in tangential velocity of the sliding particle layer with the impact angle acts to increase the rebounding speed. This reduces the difference between the measured value of $\bar{e}$ between particle-laden flows with high volume fraction relative to single particles, although the angle of the rebound is modified by the transfer in momentum from the layer.

CRediT authorship contribution statement

Shipu Han: Conceptualization, Data curation, Formal analysis, Investigation, Methodology, Writing – original draft. **Zhiwei Sun:** Conceptualization, Formal analysis, Methodology, Supervision, Writing – review & editing. **Zhao Feng Tian:** Conceptualization, Supervision, Writing – review & editing. **Alfonso Chinnici:** Conceptualization, Supervision, Writing – review & editing. **Timothy Lau:** Conceptualization, Formal analysis, Supervision, Writing – review & editing. **Maurizio Troiano:** Data curation, Formal analysis, Investigation, Supervision, Writing – review & editing. **Roberto Solimene:** Data curation, Formal analysis, Writing – review & editing. **Piero Salatino:** Project administration, Supervision, Writing – review & editing. **Graham J. Nathan:** Conceptualization, Investigation, Methodology, Project administration, Supervision, Writing – review & editing.

Declaration of competing interest

The authors declare that they have no known competing financial interests or personal relationships that could have appeared to influence the work reported in this paper.

Data availability

Data will be made available on request.

Acknowledgement

Financial supports of the Australian Research Council (DP180102045) and the US DoE through the G3-P3 project DE-FOA-0001697 are gratefully acknowledged. We also acknowledge valuable discussions from Dr. Jin-Soo Kim, Commonwealth Scientific and Industrial Research Organisation, and Dr. Clifford Ho, Sandia National Laboratory, with regard to the conditions of interest to falling particle curtain solar receivers.

Appendix A. Particle properties

Table A
Carbo CP 70/140 Particle Properties[a].

Property	Value
Composition	Sintered bauxite
Mass-median diameter, d_p (μm)	154
Diameter distribution (μm)	74–105: 5%; 105–149: 43%; 149–212: 51%; 212–300: 1%
Bulk density, ρ_{pb} (kg/m^3)	1890
Density, ρ_p (kg/m^3)	3250
Sphericity	0.8

[a] : From https://carboceramics.com

Appendix B. Surface roughness of target plates

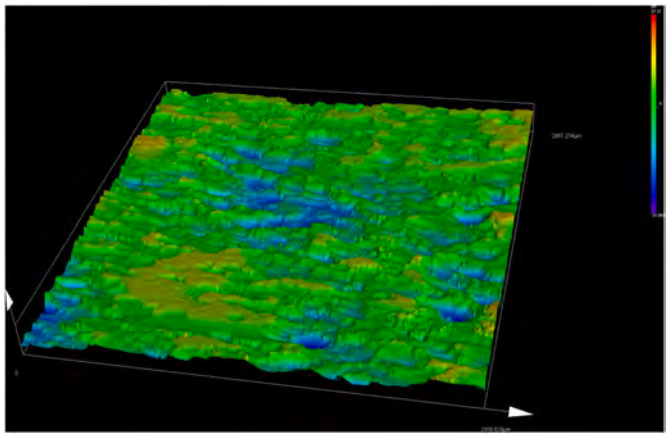

Fig. B. Scanning image of the stainless-steel plate with No 1 surface finish used in experiments collected by profilometer.

Table B
Surface roughness results of the stainless-steel plate used in experiments.

Root mean square height, Sq [μm]	Maximum peak height, Sp [μm]	Maximum pit height, Sv [μm]	Arithmetical mean height, Sa [μm]
7.187	24.385	27.861	5.805

References

[1] E. Longmire, J.K. Eaton, Structure of a particle-laden round jet, J. Fluid Mech. 236 (1992) 217–257, https://doi.org/10.1017/S002211209200140X.
[2] L. Chen, S.Z. Yong, A.F. Ghoniem, Oxy-fuel combustion of pulverized coal: characterization, fundamentals, stabilization and CFD modeling, Prog. Energy Combust. Sci. 38 (2012) 156–214, https://doi.org/10.1016/j.pecs.2011.09.003.
[3] C.K. Ho, B.D. Iverson, Review of high-temperature central receiver designs for concentrating solar power, Renew. Sust. Energ. Rev. 29 (2014) 835–846, https://doi.org/10.1016/j.rser.2013.08.099.
[4] T.C.W. Lau, J.H. Frank, G.J. Nathan, Resolving the three-dimensional structure of particles that are aerodynamically clustered by a turbulent flow, Phys. Fluids 31 (2019), https://doi.org/10.1063/1.5110323.
[5] Z.Q. Li, F. Wei, Y. Jin, Numerical simulation of pulverized coal combustion and NO formation, Chem. Eng. Sci. 58 (2003) 5161–5171, https://doi.org/10.1016/j.ces.2003.08.012.
[6] C.K. Ho, J.M. Christian, D. Romano, J. Yellowhair, N. Siegel, L. Savoldi, R. Zanino, Characterization of particle flow in a free-falling solar particle receiver, J. Sol. Energy Eng. Trans. ASME. 139 (2017) 1–9, https://doi.org/10.1115/1.4035258.
[7] M. Troiano, F. Montagnaro, P. Salatino, R. Solimene, Experimental characterization of particle-wall interaction relevant to entrained-flow gasification of biomass, Fuel 209 (2017) 674–684, https://doi.org/10.1016/j.fuel.2017.08.044.
[8] M.C. Marinack, R.E. Musgrave, C.F. Higgs, Experimental investigations on the coefficient of restitution of single particles, Tribol. Trans. 56 (2013) 572–580, https://doi.org/10.1080/10402004.2012.748233.
[9] D. Patil, C. Fred Higgs, Experimental investigations on the coefficient of restitution for sphere–thin plate elastoplastic impact, J. Tribol. 140 (2017) 011406, https://doi.org/10.1115/1.4037212.
[10] K. Yu, D. Tafti, Size and temperature dependent collision and deposition model for micron-sized sand particles, J. Turbomach. 141 (2019) 1–11, https://doi.org/10.1115/1.4042215.
[11] C.J. Reagle, J.M. Delimont, W.F. Ng, S.V. Ekkad, Study of microparticle rebound characteristics under high temperature conditions, Proc. ASME Turbo Expo. 2 (2013) 1–7, https://doi.org/10.1115/GT2013-95083.
[12] S. Wall, W. John, H.C. Wang, S.L. Goren, Measurements of kinetic energy loss for particles impacting surfaces, Aerosol Sci. Technol. 12 (1990) 926–946, https://doi.org/10.1080/02786829008959404.
[13] A. Aryaei, K. Hashemnia, K. Jafarpur, Experimental and numerical study of ball size effect on restitution coefficient in low velocity impacts, Int. J. Impact Eng. 37 (2010) 1037–1044, https://doi.org/10.1016/j.ijimpeng.2010.04.005.
[14] P.F. Dunn, R.M. Brach, G.G. Janson, Surface-contact mechanics during oblique impact of microspheres with planar surfaces, Aerosol Sci. Technol. 25 (1996) 445–465, https://doi.org/10.1080/02786829608965409.
[15] D.A. Gorham, A.H. Kharaz, The measurement of particle rebound characteristics, Powder Technol. 112 (2000) 193–202, https://doi.org/10.1016/S0032-5910(00)00293-X.
[16] J.M. Delimont, M.K. Murdock, W.F. Ng, S.V. Ekkad, Effect of temperature on microparticle rebound characteristics at constant impact velocity part 1, Proc. ASME Turbo Expo. 1A (2015) 1–9, https://doi.org/10.1115/GT2014-25687.
[17] M. Troiano, T. Santagata, F. Montagnaro, P. Salatino, R. Solimene, Impact experiments of char and ash particles relevant to entrained-flow coal gasifiers, Fuel 202 (2017) 665–674, https://doi.org/10.1016/j.fuel.2017.03.056.
[18] S. Elghobashi, On predicting particle-laden turbulent flows, Appl. Sci. Res. 52 (1994) 309–329, https://doi.org/10.1007/BF00936835.
[19] Y.J. Jiang, Y. Zhao, Experimental investigation of dry granular flow impact via both normal and tangential force measurements, Geotech. Lett. 5 (2015) 33–38, https://doi.org/10.1680/geolett.15.00003.
[20] L.E. Silbert, D. Ertaş, G.S. Grest, T.C. Halsey, D. Levine, S.J. Plimpton, Granular flow down an inclined plane: Bagnold scaling and rheology, Phys. Rev. E - Stat. Physics, Plasmas, Fluids, Relat. Interdiscip. Top. 64 (2001) 14, https://doi.org/10.1103/PhysRevE.64.051302.
[21] O. Pouliquen, Scaling laws in granular flows down rough inclined planes, Phys. Fluids 11 (1999) 542–548, https://doi.org/10.1063/1.869928.
[22] Y.J. Jiang, I. Towhata, Experimental study of dry granular flow and impact behavior against a rigid retaining wall, Rock Mech. Rock. Eng. 46 (2013) 713–729, https://doi.org/10.1007/s00603-012-0293-3.
[23] CARBO Ceramics Inc, Carbobead High-Performance Ceramic Media, 2022 https://carboceramics.com (accessed June 2, 2022).
[24] M. Troiano, R. Solimene, P. Salatino, F. Montagnaro, Multiphase flow patterns in entrained-flow slagging gasifiers: physical modelling of particle-wall impact at near-ambient conditions, Fuel Process. Technol. 141 (2016) 106–116, https://doi.org/10.1016/j.fuproc.2015.06.018.
[25] S. Puttinger, G. Holzinger, S. Pirker, Investigation of highly laden particle jet dispersion by the use of a high-speed camera and parameter-independent image analysis, Powder Technol. 234 (2013) 46–57, https://doi.org/10.1016/j.powtec.2012.09.034.
[26] T.C.W. Lau, G.J. Nathan, Influence of stokes number on the velocity and concentration distributions in particle-laden jets, J. Fluid Mech. 757 (2014) 432–457, https://doi.org/10.1017/jfm.2014.496.
[27] T.C.W. Lau, G.J. Nathan, The effect of stokes number on particle velocity and concentration distributions in a well-characterised, turbulent, co-flowing two-phase jet, J. Fluid Mech. 809 (2016) 72–110, https://doi.org/10.1017/jfm.2016.666.
[28] P.A.M. Kalt, C.H. Birzer, G.J. Nathan, Corrections to facilitate planar imaging of particle concentration in particle-laden flows using Mie scattering, part 1: collimated laser sheets, Appl. Opt. 46 (2007) 5823–5834, https://doi.org/10.1364/AO.46.007227.

[29] S. Han, Z. Sun, Z.F. Tian, T. Lau, G. Nathan, Particle velocity measurement within a free-falling particle curtain using microscopic shadow velocimetry, Opt. Express 29 (2021) 10923, https://doi.org/10.1364/oe.421017.
[30] A. Sciacchitano, B. Wieneke, F. Scarano, PIV uncertainty quantification by image matching, Meas. Sci. Technol. 24 (2013), https://doi.org/10.1088/0957-0233/24/4/045302.
[31] N. Sedaghatizadeh, M. Arjomandi, T. Lau, G. Nathan, The dominant underlying parameters controlling the dispersion of falling particle curtains, Powder Technol. 402 (2022) 117343, https://doi.org/10.1016/j.powtec.2022.117343.
[32] Z. Liu, P. Cooper, P.W. Wypych, Air entrainment by free falling streams of particles, in: Australas. Fluid Mech. Conf, 2004.
[33] R. Delannay, A. Valance, A. Mangeney, O. Roche, P. Richard, Granular and particle-laden flows: from laboratory experiments to field observations, J. Phys. D. Appl. Phys. 50 (2017) 53001, https://doi.org/10.1088/1361-6463/50/5/053001.
[34] M. Sommerfeld, N. Huber, Experimental analysis of modelling of particle-wall collisions, Int. J. Multiphase Flow 25 (1999) 1457–1489, https://doi.org/10.1016/S0301-9322(99)00047-6.
[35] F. Bourrier, F. Nicot, F. Darve, Physical processes within a 2D granular layer during an impact, Granul. Matter 10 (2008) 415–437, https://doi.org/10.1007/s10035-008-0108-0.
[36] J.M. Delimont, M.K. Murdock, W.F. Ng, S.V. Ekkad, Effect of temperature on microparticle rebound characteristics at constant impact velocity part 2, Proc. ASME Turbo Expo. 1A (2015), https://doi.org/10.1115/GT2014-25687.